This article has been accepted for publication in a future issue of this journal, but has not been fully edited. Content may change prior to final publication. Citation information: DOI 10.1109/TMI.2015.2425144, IEEE Transactions on Medical Imaging

Multiple LREK Active Contours for Knee Meniscus Ultrasound Image Segmentation

Amir Faisal, Siew-Cheok Ng, Siew-Li Goh, John George, Eko Supriyanto, and Khin W. Lai

***Abstract*—Quantification of knee meniscus degeneration and displacement in an ultrasound image requires simultaneous segmentation of femoral condyle, meniscus, and tibial plateau in order to determine the area and the position of the meniscus. In this paper, we present an active contour for image segmentation that uses scalable local regional information on expandable kernel (LREK). It includes using a strategy to adapt the size of a local window in order to avoid being confined locally in a homogeneous region during the segmentation process. We also provide a multiple active contours framework called multiple LREK (MLREK) to deal with multiple object segmentation without merging and overlapping between the neighbouring contours in the shared boundaries of separate regions. We compare its performance to other existing active contour models and show an improvement offered by our model. We then investigate the choice of various parameters in the proposed framework in response to the segmentation outcome. Dice coefficient and Hausdorff distance measures over a set of real knee meniscus ultrasound images indicate a potential application of MLREK for assessment of knee meniscus degeneration and displacement.**

***Index Terms*—Knee joint, meniscus, ultrasound, image segmentation, active contour, level set, multiregion segmentation.**

I. Introduction

OSTEOARTHRITIS (OA) is the most common form of arthritis where the knee is the most studied joint [1]. Knee OA is recognized as a disease involving entire joint structure, including bone, cartilage, meniscus, ligament, synovium, and synovial fluid where visualization of these structures is necessary for a complete assessment [2]. X-rays, which are useful to depict bony structures, have been used to provide an indirect measurement of knee cartilage thickness through the distance between femur and tibia [3]. It is known that the joint space is also shared by meniscus where its degeneration and displacement contribute to knee OA progression as well [4]-[6]. However, x-rays lack depiction of soft tissue. On the other hand, magnetic resonance imaging (MRI) allows entire joint structure assessment and has been used as a reliable and sensitive knee OA diagnostic tool [18] where a variety of approaches in segmenting bone, cartilage, and meniscus are using this imagery [7]-[14]. Nonetheless, high cost, high time consumption, and low availability of the equipment limit its routine clinical use [19].

Although the nature of sound prevents penetration into the deep articular structure and subchondral bone, ultrasound has shown its ability in visualizing more OA appearance features than x-rays [15], such as cartilage loss [16], meniscal tears [17], ligament damage [18], and synovial proliferation [18]. Ultrasound, which is more affordable and widely accessible than MRI, can be used as an excellent alternative to help diagnose the presence of knee OA disease [19]. In order to quantify knee meniscus degeneration and displacement, it is necessary to segment various parts of knee joints in an ultrasound image. While boundary delineation of only meniscus determines its area deformation, detection of meniscus displacement requires information on the relative position of the meniscus in relation to the femoral condyle and the tibial plateau. The goal in the knee meniscus ultrasound image segmentation is to simultaneously capture multiple objects, including the femoral condyle, the meniscus, and the tibial plateau of the knee joint. The segmentation algorithm should include the objects separately without merging and overlapping between adjacent contours in the shared boundaries of disjointed objects. It should also be insensitive to various shapes of the objects as well as to speckle noise which varies the contrast of the object.

Active contours have been extensively used in addressing medical image segmentation problems. In general, they can be categorized into global and local active contour models. To locate an object's boundary, the global models take into account entire image intensity [20], [21], whereas the local models use either local edge pixels [22] or local intensity pixels [23], [24]. The sensitivity of global models to initial conditions may not be desirable in the case of capturing the multiple objects due to its tendency to capture entire image structures where various positions of an initial contour just evolves into a similar final position [20], [21]. The sensitivity of the local models to initial conditions constrains the initial contour to reside in close vicinity of the object [22], [23], on the other hand, allows segmentation of obtaining different objects of interest by placing different positions of the initial contour, thus allowing separation of a particular object from the rest of the image structures. As speckling causes faulty edge points, it often prevents the edge-based models from evolving into the real boundary. The robustness of the local

Manuscript received October 16, 2014; revised April 16, 2015; accepted April 19, 2015. This work was supported in part by the University of Malaya Research Grant (RP020A-13AET), in part by the International Graduate Research Assistantship Scheme, and in part by the Postgraduate Research Grant (PG003-2014B). The associate editor coordinating the review of this manuscript and approving it for publication was Prof. Terry M. Petters.

A. Faisal, S. C. Ng, and K. W. Lai are with the Department of Biomedical Engineering, University of Malaya, 50603 Kuala Lumpur, Malaysia (e-mail: amirf415al@yahoo.com; siewcng@um.edu.my; lai.khinwee@um.edu.my).

S. L. Goh and J. George are with the Faculty of Medicine, University of Malaya, 50603 Kuala Lumpur, Malaysia (e-mail: gsiewli@um.edu.my; johng_rad@um.edu.my).

E. Supriyanto is with the Faculty of Biosciences and Medical Engineering, University of Technology, Malaysia, 81310 Johor Bahru, Malaysia (e-mail: eko@biomedical.utm.my).

This article has been accepted for publication in a future issue of this journal, but has not been fully edited. Content may change prior to final publication. Citation information: DOI 10.1109/TMI.2015.2425144, IEEE Transactions on Medical Imaging

regional model against noises is likely to provide a desirable outcome as it employs intensity instead of edge pixels [23].

There exist several newly proposed active contours using local regional descriptor such as localizing region-based active contour (LRAC) [23], local regional descriptor for active contour evolutions (LRD) [24], and active contour using local regional information on extendable search lines (LRES) [25]. LRAC, LRD, and LRES re-formulate the regional statistics to sample local intensity only within fixed-radius balls, fixed-scale square windows, and extendable search lines along the evolving contour, respectively. In LRAC, an appropriate scale needs to be manually set, depending on the distance between the position of the initial contour and the location of the object. If the initial contour is placed too far from the nearest boundary and the scale is too small, the contour may not completely penetrate the boundary or any concave parts. To deal with the local minima problem, LRD adds the balloon force and introduces two novel segmenter functions. However, both schemes require that the initial contour be placed entirely inside the object of interest only. LRES employs extendable search lines that are perpendicular to the contour front to reach the concave-shaped boundary. The area of long, thin search lines is not scalable to an image area. Also, insufficient statistics inside the lines may navigate the contour wrongly.

In order to avoid being confined locally in a homogeneous region during the segmentation process, we use a strategy inside the variational level set method to adapt the size of a local window. It uses intensity values of the pixels on a set of scalable kernels along the evolving contour to direct the contour's front towards the object's boundary within an image domain. The support of each kernel is defined one at a time in each of the points along the contour. During the level set evolution, the scale of this local neighbourhood varies for each contour point and is dependent on the distance of this point to the nearest boundary. The estimation of the kernel size is influenced by the local image intensity and not performed on the whole image, but only on the zero level of the contour.

This paper presents multiple active contours using scalable local regional information on expandable kernel (MLREK) for knee meniscus ultrasound image segmentation. We start by describing an active contour with the variable scale kernel to navigate the contour towards the object boundary within the image domain. We then provide the multiple level set formulation to the proposed framework to deal with simultaneous multiple object segmentation without merging and overlapping between adjacent contours. Next, we compare different active contour models in terms of segmentation results, speed, and convergence properties. We also investigate various parameters in the proposed method and their effects on the segmentation results. Finally, we present the application of MLREK for the knee meniscus ultrasound image segmentation as an initial step to measure the degeneration and displacement.

II. Multiple LREK Active Contours

A. Scalable Local Regional Information

Let I denote an input image defined on an image spatial domain Ω. The evolving contour at time t, $C(t) \subset \Omega$ is to be embedded as the zero level set of a function $\phi(\mathbf{x}) : \Omega \rightarrow \Re$, where $\Re$ is a set of real numbers.

$$C(t) = \{\mathbf{x} \in \Omega : \phi(\mathbf{x}, t) = 0\} \text{ with } C_0 = \phi(\mathbf{x}, 0) \quad (1)$$

where C_0 is the initial contour.

The region inside, outside, and around the contour are represented by the regularized Heaviside function H_ϵ, $(1 - H_\epsilon)$, and the smoothed Dirac delta function $\delta_\epsilon = H'_\epsilon$, respectively. H_ϵ and δ_ϵ are computed by (2) and (3) with $\epsilon = 1$ as in [20], respectively.

$$H_\epsilon(\phi) = \frac{1}{2}\left(1 + \frac{2}{\pi}\arctan\left(\frac{\phi}{\epsilon}\right)\right) \quad (2)$$

$$\delta_\epsilon(\phi) = \frac{1}{\pi}\left(\frac{\epsilon}{\pi^2 + \phi^2}\right). \quad (3)$$

We define a scalable local regional (SLR) information as an image's weighted intensity average within an expandable kernel. The kernel is used to mask the local intensity region. We choose the kernel function as the uniform kernel, $K_u(d) = c$, where $d = \|\mathbf{x} - \mathbf{y}\|$ is L_2-norm distance between the kernel center point $\mathbf{x}$ which is on the contour pixels and other pixels $\mathbf{y}$ within the kernel support and c is a positive constant. The contour line divides each kernel into two regions that are inside and outside the contour to measure the intensity profiles $I(\mathbf{x})$ at image pixel $\mathbf{x}$ on both regions.

The SLR energy function, as given in (4), considers pixel contributions within the distance, d, from the contour and ignores any spatial intensity variation outside the distance, d. This local version of the Chan-Vese energy [20] obtains its optimum point when the contour has arrived at the point where the intensity profile within the kernel at each contour point $I(\mathbf{x})$ is approximated by their local means μ_{in} and μ_{out}, obtained using equations in (5) and (6), respectively.

$$\begin{aligned} E_{\text{SLR}}(\phi) \quad = \quad & \int_\Omega K(\|\mathbf{x} - \mathbf{y}\|)\Big(|I(\mathbf{x}) - \mu_{\text{in}}|^2 H_\epsilon(\phi(\mathbf{x})) \\ & + |I(\mathbf{x}) - \mu_{\text{out}}|^2 (1 - H_\epsilon(\phi(\mathbf{x})))\Big) d\mathbf{x} \end{aligned} \quad (4)$$

where

$$\mu_{\text{in}} = \frac{\int_\Omega K(\|\mathbf{x} - \mathbf{y}\|) H_\epsilon(\phi(\mathbf{x})) I(\mathbf{x}) d\mathbf{x}}{\int_\Omega K(\|\mathbf{x} - \mathbf{y}\|) H_\epsilon(\phi(\mathbf{x})) d\mathbf{x}} \quad (5)$$

$$\mu_{\text{out}} = \frac{\int_\Omega K(\|\mathbf{x} - \mathbf{y}\|)(1 - H_\epsilon(\phi(\mathbf{x}))) I(\mathbf{x}) d\mathbf{x}}{\int_\Omega K(\|\mathbf{x} - \mathbf{y}\|)(1 - H_\epsilon(\phi(\mathbf{x}))) d\mathbf{x}} \quad (6)$$

are means intensities of inner and outer areas of the expandable kernel, respectively.

An LREK contour's energy function formulated using the level set function is given in (7). In the first term of (7), multiplication of the E_{SLR} with δ_ϵ ensures no sudden development of new contours while keeping it topologically flexible. To regulate the contour's elasticity, the second term of (7) computes the arc length of the zero level set.

$$\begin{aligned} E(\phi) \quad = \quad & -\int_\Omega \Big(\delta_\epsilon(\phi(\mathbf{y})) E_{\text{SLR}}(\phi(\mathbf{x})) \\ & - \nu \delta_\epsilon(\phi(\mathbf{y})) |\nabla \phi(\mathbf{y})| \Big) d\mathbf{y}. \end{aligned} \quad (7)$$

This article has been accepted for publication in a future issue of this journal, but has not been fully edited. Content may change prior to final publication. Citation information: DOI 10.1109/TMI.2015.2425144, IEEE Transactions on Medical Imaging

Using the standard gradient descent method, the minimization of $E(\phi)$ in (7) with respect to ϕ can be performed by solving the gradient flow equation $\frac{\partial \phi}{\partial t} = -\frac{\partial E}{\partial \phi}$. The derivation of $\frac{\partial E}{\partial \phi}$ is obtained using the Gateau derivative, which is detailed more in the Appendix. It is accomplished by replacing ϕ with $\phi+\xi\psi$, where ψ denotes a tiny change perpendicular to ϕ weighted with a small number ξ. The corresponding gradient flow equation is expressed in (8) which is composed of the SLR force that behaves as an attractor to move the center of each kernel which is the contour and the contour's length regulation term serving to smoothen the contour, respectively.

$$\frac{\partial \phi}{\partial t} = \delta_\epsilon(\phi(\mathbf{y}))\left(F_{\mathrm{SLR}}(\phi(\mathbf{x})) + \nu \mathrm{div}\left(\frac{\nabla\phi(\mathbf{y})}{|\nabla\phi(\mathbf{y})|}\right)\right) \tag{8}$$

$$\begin{aligned} F_{\mathrm{SLR}}(\phi(\mathbf{x})) \quad &= \quad \int_\Omega \delta_\epsilon(\phi(\mathbf{x}))K(\|\mathbf{x}-\mathbf{y}\|) \\ &\quad \times \left(|I(\mathbf{x})-\mu_{\mathrm{in}}|^2 - |I(\mathbf{x})-\mu_{\mathrm{out}}|^2\right) d\mathbf{x}. \end{aligned} \tag{9}$$

We devise a strategy to prevent the contour from being trapped in local minima. Let each kernel be of scale d_k, $k = 1, 2, \ldots, m$ defined at the contour points k, where m is the number of pixels on the contour. The number of kernels thus depends on the number of pixels on the contour in each iteration. The scale of each kernel is initially set to $d_k = d_{\mathrm{initial}}$ pixels and adaptable throughout the evolution process which is enabled by gradually adding Δd pixels to d for each point along the contour. This scale adaptation relies on the comparison of the absolute difference of μ_{in} and μ_{out} to a threshold value thres. This is to indicate whether the kernel is still in the homogeneous area of the object or the background or has reached the boundary of the object. $\mathrm{thres} = [L \times \tau]$ represents a small percentage of the intensity value range of the given image where $\tau \subseteq [0, 1]$ and $L = 255$ for 8-bit grayscale images. This value should be kept near zero to indicate that μ_{in} is different from μ_{out}. If the kernel lies entirely in the homogeneous area, it means their absolute difference is less than the threshold where μ_{in} is about the same as μ_{out}. In this case, the support of the kernel is gradually expanded for each contour point. This process is iterated until the kernel has reached the nearest boundary covering both the object and background areas. Once it has found a non-homogeneous region or crosses some parts of the boundary, μ_{in} is significantly different from μ_{out} in which the absolute difference is larger than the threshold. It implies that the kernel has found its optimum scale, thus the SLR force determines the motion of the contour line to meet the boundary.

According to (9), the SLR force will navigate the contour in either inward or outward direction influenced by the difference between $I(\mathbf{x})$ and μ_{in} or μ_{out}. If the value of $I(\mathbf{x})$ is closer to μ_{in} than μ_{out}, the negative sign of the SLR force will drive the contour outward. If $I(\mathbf{x})$ is about the same value as μ_{out} and far different from μ_{in}, the positive sign of the SLR force will push the contour front inward. The contour converges at the boundary when the value of $I(\mathbf{x})$ is about the same either with μ_{in} or μ_{out}. In other words, the SLR force gives zero value and will not induce motion force any longer.

B. Multiple Level Set Formulation

Several multiphase level set frameworks deal with multiple region segmentation using global regional descriptor [26], [27]. The framework in [26] assigns n-level set functions to represent 2^n regions. It does not need an additional constraint as the junctions between multiple contours represent the regions to be segmented. If the number of the regions is not a power of two, it produces empty regions as a particular region is weighted twice. The framework in [27] represents each object's region with one level set function and allows the coupled contours to compete with each other and move according to the strongest force. If no competing region exists, an additional term is used to grow the contour towards the vacuum area with a constant speed. Inspired by this assumption, LRAC [23] formulates its multiple level set scheme using its local regional descriptor by letting interacting contours compete at their interfaces to avoid overlaps. The coupled level set method in [28] handles junctions between several curves of level set using an additional constraint. In addition to the length and area terms, they place a third term, $\int \frac{\lambda}{2}\left(\sum_{i=1}^{n} H(\phi_i(\mathbf{x})) - 1\right)^2 d\mathbf{x}$ into their energy function. In their gradient flow equation, the term $\lambda\left(\sum_{j=1}^{n} H(\phi_j(\mathbf{x})) - 1\right)$ is used to avoid the growth of overlap or vacuum regions between the neighbouring curves, where λ is a Lagrange multiplier and $1 \leq i < j \leq n$. As this term forces the junctions to vanish, the adjacent curves thus share the border.

We start to re-formulate the previous energy function into an n-active contours framework to allow simultaneous multiple region segmentation. We see that the formulation in Section II-A is for the case of $n = 1$ represented by only one level set function. To segment object regions with $n > 1$, we can use two or more level set functions $\phi_1, \ldots, \phi_n$. Then, n-level set functions $(\phi_i)_{i=1}^n$ are used to embed multiple contours where each of the level set functions represents one object's region. Thus, the previous single level sets energy functions in (7) can be converted into multiple level sets formulae as follows, considering the number of regions, n, is known.

$$\begin{aligned} E(\phi_1, \ldots, \phi_n) \quad &= \quad -\int_\Omega \sum_{i=1}^{n} \Big(\delta_\epsilon(\phi_i(\mathbf{y})) E_{\mathrm{SLR}}(\phi_i(\mathbf{x})) \\ &\qquad -\nu\delta_\epsilon(\phi_i(\mathbf{y}))|\nabla\phi_i(\mathbf{y})| \Big) d\mathbf{y}. \end{aligned} \tag{10}$$

To prevent multiple level set functions from overlapping with one another, an additional constraint is needed to regulate the zero level contour. To segment multiple objects with shared boundaries, we are inspired by the strategy in [28] and it is modified to be utilized with the scalable local regional information. Therefore, we place an additional constraint as the third term in the total energy function. We write the multiple level set formulation of MLREK's energy using a vector value notation $\Phi = (\phi_1, \ldots, \phi_n)$ as given in (11).

By minimizing the MLREK energy function in (11) with respect to Φ, we obtain the gradient equation flow in (12) for $\phi_i; i = 1, \ldots, n$. The corresponding gradient flow equation evolving every level set function ϕ_i is defined in (13). In equation (12), the first term is the SLR force, the second term is the contour smoothing force, and the third term is the area term of

This article has been accepted for publication in a future issue of this journal, but has not been fully edited. Content may change prior to final publication. Citation information: DOI 10.1109/TMI.2015.2425144, IEEE Transactions on Medical Imaging

$$E(\Phi) = -\int_{\Omega}\left(\delta_{\epsilon}(\Phi(\mathbf{y}))E_{\mathrm{SLR}}(\Phi(\mathbf{x})) - \nu\delta_{\epsilon}(\Phi(\mathbf{y}))|\nabla\Phi(\mathbf{y})| - \sum_{p\neq i}^{n} H_{\epsilon}(\Phi(\mathbf{y}))H_{\epsilon}(\Phi_p(\mathbf{y}))\right)d\mathbf{y} \tag{11}$$

$$\frac{\partial\phi_i}{\partial t} = \delta_{\epsilon}(\phi_i(\mathbf{y}))\left(F_{\mathrm{SLR}}(\phi_i(\mathbf{x})) + \nu\mathrm{div}\left(\frac{\nabla\phi_i(\mathbf{y})}{|\nabla\phi_i(\mathbf{y})|}\right) + \sum_{p\neq i}^{n} H_{\epsilon}(\phi_p(\mathbf{y}))\right). \tag{12}$$

the regularized Heaviside functions. The third term is used to prevent the neighbouring contours from creating overlapping regions. When updating the contour ϕ_i, other contours $(\phi_p)_{p\neq i}^{n}$ are represented by their area terms $\sum_{p\neq i}^{n} H_{\epsilon}(\phi_p(\mathbf{y}))$ where $H_{\epsilon}(\phi)$ is computed according to equation (2). This strategy thus avoids the evolving contours from surpassing each other in the shared boundaries of disjointed regions.

$$\begin{aligned}
\frac{\partial\phi_1}{\partial t} &= \delta_{\epsilon}(\phi_1(\mathbf{y}))\left(F_{\mathrm{SLR}}(\phi_1(\mathbf{x})) + \nu\mathrm{div}\left(\frac{\nabla\phi_1(\mathbf{y})}{|\nabla\phi_1(\mathbf{y})|}\right) + \sum_{p\neq 1}^{n} H_{\epsilon}(\phi_p(\mathbf{y}))\right)\\
&\vdots\\
\frac{\partial\phi_n}{\partial t} &= \delta_{\epsilon}(\phi_n(\mathbf{y}))\left(F_{\mathrm{SLR}}(\phi_n(\mathbf{x})) + \nu\mathrm{div}\left(\frac{\nabla\phi_n(\mathbf{y})}{|\nabla\phi_n(\mathbf{y})|}\right) + \sum_{p\neq n}^{n} H_{\epsilon}(\phi_p(\mathbf{y}))\right).
\end{aligned} \tag{13}$$

C. Evolution Process

The evolution process of MLREK begins by setting number of iterations l, multiple positions of initial contour C_0, initial scale of the kernel d_{initial}, its additional scale Δd, and threshold value thres. Each of the contours C_i is embedded in the zero level set function $\phi_i; i = 1, \ldots, n$ where n represents the number of the contours and the object's region. For $i = 1, \ldots, n$, the value of d_i, Δd_i, and thres_i can be different and is not necessarily set to be similar for each function ϕ_i.

As the energy is minimized by an iterative process, the zero level of contours ϕ_i is updated at each time step $j = 1, \ldots, l$. For every contour point $k = 1, \ldots, m$, we set $d_k = d_{\mathrm{initial}}$. We compute μ_{in} and μ_{out} using equations in (5) and (6), respectively. Then, we check the condition $|\mu_{\mathrm{in}} - \mu_{\mathrm{out}}| < \mathrm{thres}$ where $|.|$ denotes absolute value. If the condition is true, we set $d_k = d_k + \Delta d$, proceed to update μ_{in} and μ_{out}, and return to check the condition. It will be repeated until the condition is not met, and then we can proceed to compute F_{SLR}. All of these processes are iteratively repeated for every kernel on the contour point. Then, the contour ϕ_i is navigated towards the boundary using (9). Its smoothness is enforced by the second term of (12). Meanwhile, other contours $(\phi_p)_{p\neq i}^{n}$ are described by their area terms $\sum_{p\neq i}^{n} H_{\epsilon}(\phi_p(\mathbf{y}))$. Another contour's evolution starts by re-initializing d_k to d_{initial} and repeating the whole process. Then, all contours are evolved by one iteration and will be reiterated until the contours converge to the boundary or a maximum number of iterations is reached. The entire evolution process is illustrated in Algorithm 1.

Algorithm 1 MLREK's evolution process

```
Set l, d_i, Δd_i, thres_i, and φ_i for i = 1, ..., n;
m is number of points in φ;
for j ← 1, l do                          ▷ Loop until l iteration numbers
    for i ← 1, n do                      ▷ Loop for n contours
        for k ← 1, m do                  ▷ Loop for m contour points
            Set d_k = d_initial          ▷ Set initial kernel's scale
            Compute μ_in and μ_out according to (5) and (6)
            while |μ_in − μ_out| < thres do
                Set d_k = d_k + Δd       ▷ Expand the kernel
                Update μ_in and μ_out
            end while
            Compute F_SLR according to (9)
        end for
        Evolve φ_i according to (12)
    end for
end for
```

III. Data Acquisition

We utilized the Philips ClearVue 550 ultrasound system with a 2D, 12 MHz (L12-4) broadband linear array transducer. The high frequency transducer is desirable to capture superficial periarticular and intraarticular structures [29]. In order to observe the medial meniscus, the medial side of the anterior view of the knee joint of the subject was scanned in vivo with the supine position and the knee flexed 90°. 19 asymptomatic subjects (15 males and 4 females, age range: 18-55 years, mean age: 31.20 ± 14.41) were recruited with an informed consent. The acquisition was performed by a professional sonographer in Ultrasound Room, Department of Biomedical Imaging, University of Malaya Medical Center, Kuala Lumpur, Malaysia. The study was approved by the University of Malaya Medical Ethics Committee (MECID No. 20147-396).

IV. Results and Discussion

We conducted several experiments in order to evaluate the performance of the proposed method. First, we compared it to other active contour models in terms of segmentation results, speed, and convergence properties. Second, we studied the response in the segmentation results by varying several parameters in the proposed method. We investigated the effects of threshold value selection in response to segmentation results as well as convergence properties. We followed this with a demonstration on how the presented multiple level set framework can avoid merging and overlapping between the neighbouring contours. We then showed that different choices

This article has been accepted for publication in a future issue of this journal, but has not been fully edited. Content may change prior to final publication. Citation information: DOI 10.1109/TMI.2015.2425144, IEEE Transactions on Medical Imaging

of scale parameters can be assigned for each zero level contour in multiple region segmentation and the accuracy improvement that can be achieved. Third, we examined its application for the knee meniscus ultrasound image segmentation.

We illustrated the segmentation performance with Dice similarity coefficient (DSC) and Hausdorff distance (HD) metrics. To measure area similarity between the pixel region within a segmented contour (A) and within a reference contour (B), $DSC \in [0,1]$ is defined as the ratio between twice of the common pixel region of the segmented and reference contours and the sum of individual regions, i.e.,

$$DSC(A,B) = \frac{2|A \cap B|}{|A| + |B|}, \tag{14}$$

If DSC indicates the value of 1, it implies that A and B have the same location and size (or area). To compare the difference in shapes rather than the relative locations and sizes of the contour pair, HD in (15) measures the furthest pixel distance of the point of X from any point of Y.

$$HD(X,Y) = \max\left(\max_{x\in X}\min_{y\in Y}\|x-y\|, \max_{y\in Y}\min_{x\in X}\|x-y\|\right), \tag{15}$$

where X and Y are two sets of points extracted from the boundaries of A and B, respectively.

A. Comparison With Other Active Contour Models

In this subsection, we compared the performance of LREK to other active contour models in segmenting knee meniscus ultrasound images. From existing global regional, edge-based, and local regional active contour models, we picked a region-scalable fitting model (RSF) [21], geodesic active contour (GAC) [22], and LRAC and LRES, respectively. As depicted in Fig. 1, the meniscus located in the upper-middle of the femoral condyle and tibial plateau has a shape with deep concavity. The initial contour is placed similarly for all of the tested methods as in Fig. 1 (a). Fig. 1 (b)-(f) depict the final contours of RSF, GAC, LRAC, LRES, and LREK overlaid on the original image. To evaluate the accuracy and convergence rate, we used the segmentation result of LREK in Fig. 1 (f) as the reference to compute DSC over 1000 iterations as plotted in Fig. 2, where x and y-axes represent iteration number and DSC, respectively. We also presented computational time required by different active contour models in the Table I.

With the scale of Gaussian kernel $\sigma_K = 17$, RSF considers local intensity and handles non-uniform intensity well. Convolving the local window to the entire image leads to partitioning the brighter intensity as the object while the darker one as the background. It is unable to locate the meniscus as the only desirable object among other surroundings.

Active contours with local information are sensitive to initial contour positions which are required to be placed near the object. This limitation, on the other hand, gives advantages in obtaining a particular object among other undesired objects, depending on its initial position. They do not have a tendency to capture the entire object as opposed to RSF that partitions the image into bright and dark intensities.

To navigate the contour towards the object's edge, GAC relies on the image gradient. The speckle, often considered as

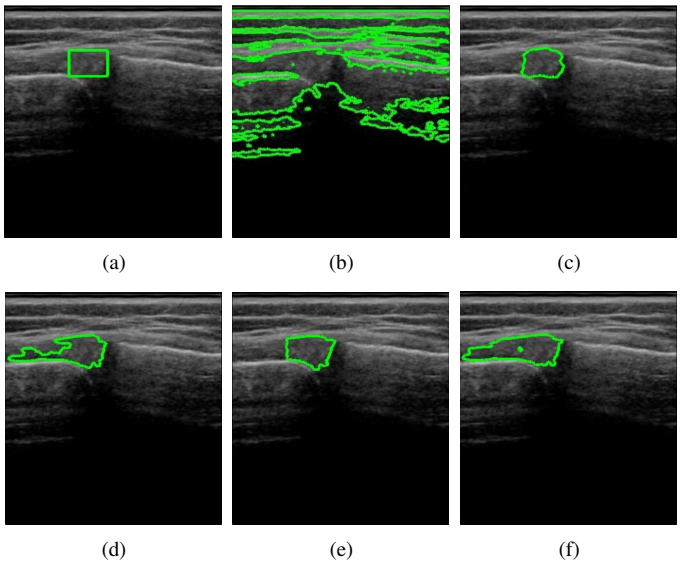

Fig. 1. Segmentation results of the meniscus (green): (a) initial contour, final contour for (b) RSF ($\sigma_K = 17$), (c) GAC ($\alpha = 0$), (d) LRAC ($r = 10$), (e) LRES ($s = 15, \Delta s = 5$, thres $= 5$), and (f) LREK ($d = 10, \Delta d = 5$, thres $= 3$), respectively. Image size is 288 $\times$ 364 pixels.

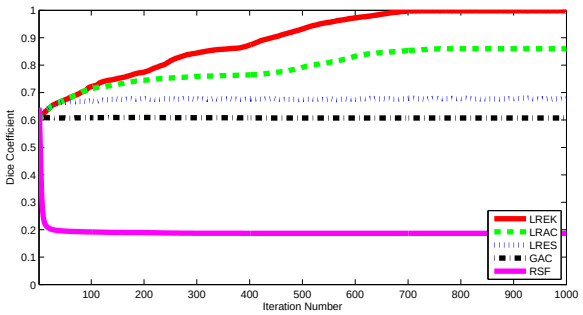

Fig. 2. Convergence properties (from bottom up) of RSF, GAC, LRES, LRAC, and LREK active contours in segmenting the meniscus.

false edge points, may prevent GAC from reaching the real boundary. Balloon force ($\alpha = 0$) can grow the contour either inward or outward direction with a small capture range and slow convergence, which impedes from penetrating into the boundary concavity of the meniscus. Another choice of α can help to gain a larger capture range, but making it sensitive to initial position. The contour may also pass through weak boundaries, particularly in the images with low contrast.

As active contours using local regional descriptors employ pixel intensity instead of edge pixels, they are more robust against noise [23]. They de-emphasize the role of image noise by computing intensity statistics within the local window. The contour can still evolve towards the boundary, although in the presence of noise. LRAC provides a more complete boundary than GAC although some areas are still excluded as segmentation outcomes. In the shared boundaries between the femoral condyle and the meniscus, the contour evolves reaching the left part of the meniscus. Meanwhile, it only arrives at the half boundary of the upper part. With $r = 10$, the distance between the contour as the center of the circle and

This article has been accepted for publication in a future issue of this journal, but has not been fully edited. Content may change prior to final publication. Citation information: DOI 10.1109/TMI.2015.2425144, IEEE Transactions on Medical Imaging

TABLE I
COMPUTATIONAL TIME OF THE DIFFERENT MODELS

Models	Total Time (s)
RSF	1,070
GAC	1,958
LRAC	215
LRES	7,630
LREK	232

the boundary is too far. The problem of limited capture range prevents the contour from evolving into the middle area of the meniscus which is considered as a homogeneous area. LRES, which utilizes extendable search lines for handling concave parts, is able to segment only into half of the meniscus area. In such low contrast images, the contour is confined in the middle area of the meniscus as shown in Fig. 1 (e). This is because the statistics on the long, thin search line may not reliably describe the local intensity to generate enough force to penetrate the other part of the meniscus.

We ran RSF, GAC, LRAC, LRES, and LREK iterate for 1000 iterations, plotted their DSC values in Fig. 2, and summarized their computational time in Table I. According to Fig. 2, they converge at approximately 50, 100, 750, 150, and 700 iterations. Instead of locating the meniscus, RSF partitions the entire image. LREK converges faster than LRAC, yet gives more complete boundaries. Although its initial scale is set to 10 pixels similar to that of LRAC, the feature of expandable kernels results in a larger capture range to propagate into the concave boundary of the meniscus as confirmed by the higher value of DSC in Fig. 2. Some other models result in less complete boundaries due to their inability to move into the concave shape, thus giving smaller values of DSC. With the speed of 7.63 seconds per iteration, LRES produces time consuming performance. It requires more computational steps to form two separate line regions inside and outside the contour and also to extend each of them as compared to LREK that just uses one kernel to form two local regions split by the contour line and to be expanded. This helps LREK to converge towards the intended boundary more rapidly than LRES. In addition, the scalability of the kernel to image size leads to a proportional computation in either small or large images. The total computational time required for RSF, GAC, LRAC, LRES, LREK to converge are 53.52, 195.79, 161.18, 1,144.49, and 162.47 seconds, respectively.

B. Further Evaluations of the Proposed Model

1) Analysing the Threshold Value: We performed another experiment to investigate the choice of the threshold value thres, a key parameter in adapting the kernel size, in response to the segmentation accuracy. We tested the performance of the single level formulation with various threshold values in segmenting a concave object of the meniscus. For this image, we varied 8 different values of thres from 3 to 17 while setting other parameters as $d = 10$ and $\Delta d = 5$ and plotted their final contours in Fig. 3. We computed DSC using the segmentation result in Fig. 3 (a) as the reference. The corresponding DSC

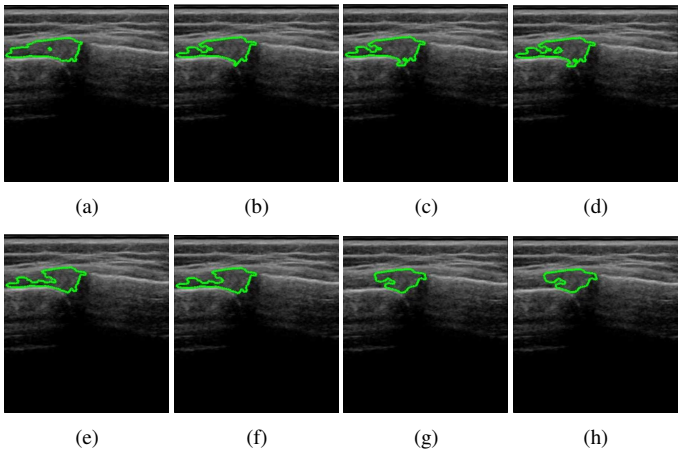

Fig. 3. (a)-(h) Shows segmentation results of LREK active contour on the meniscus (green) with $\mathrm{thres} = 3, 5, 7, 9, 11, 13, 15,$ and 17, respectively. Parameters $d = 10$, $\Delta d = 5$, and $l = 1000$. Image size is 288 $\times$ 364 pixels.

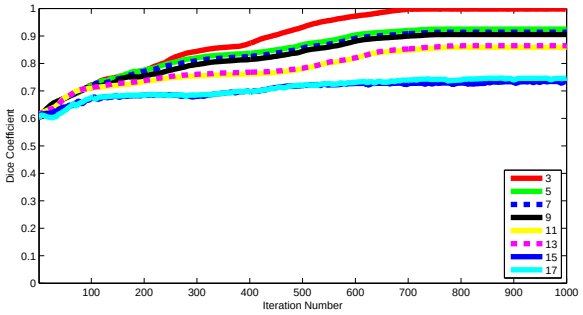

Fig. 4. Convergence properties of LREK active contour for different values of threshold in segmenting the meniscus.

values for these 8 results are plotted over the number of iterations in Fig. 4. It shows that the smallest value results in a more complete boundary of the meniscus. Meanwhile, the higher value of this parameter results in a less complete boundary. The two highest threshold values take the shortest time to converge at the same speed, however, into the least inaccurate segmentation. Two groups of intermediate values converge into two different speeds and segmentation accuracies. The first group with larger values converge faster, but into a less accurate outcome than the second group with smaller values. The smallest threshold value gives the lowest speed, but the most accurate outcome. This is because the contour requires more time to penetrate into the concave boundary. In essence, this experiment illustrates that the smallest threshold value enables the adaptation of the size of the kernel in order to detect the nearest boundary. The bigger value results in less ability of the kernel to expand and penetrate particular areas. Hence, the user may select a small threshold value to enable this feature and vice versa.

2) Multiple Region Segmentation: This experiment demonstrates multiple object segmentation using single and multiple level set formulation without and with the additional constraint according to equations (7), (10), and (11), respectively. The goal is to partition image pixels into separate objects of femoral condyle, (FC), meniscus (M), and tibial plateau (TP).

This article has been accepted for publication in a future issue of this journal, but has not been fully edited. Content may change prior to final publication. Citation information: DOI 10.1109/TMI.2015.2425144, IEEE Transactions on Medical Imaging

In Fig. 5 (b), each initial contour is placed in each object. For the result in (d), three initial contours are embedded in a single level set function ϕ. Although the final contours are shown to locate each object with different positions, they do not provide a complete separate boundary between the meniscus and the tibial plateau. As multiple objects reside close to each other, merging between adjacent contours occurs in the shared boundaries which is undesirable in this case.

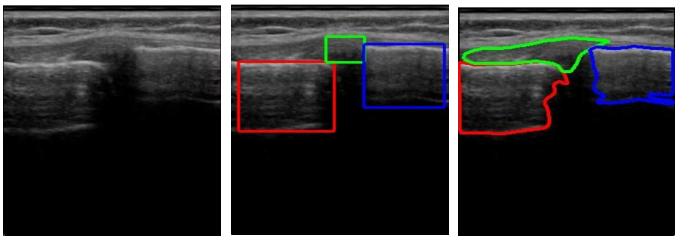

(a) Original image (b) Initial contours (c) Manually traced contours

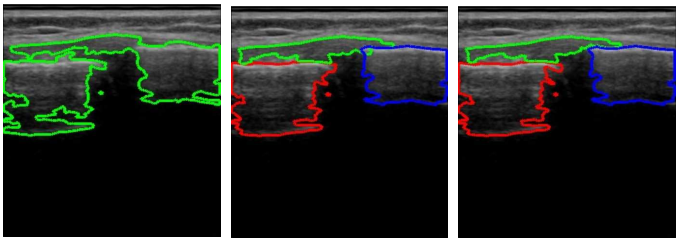

(d) Final contours obtained by single level set (e) Final contours obtained by multiple level set without constraint (f) Final contours obtained by multiple level set with constraint

Fig. 5. Simultaneous segmentation of the femoral condyle (red), the meniscus (green), and the tibial plateau (blue) with parameters ($d = 15$ and $\Delta d = 3$) for (c), ($d_{\mathrm{FC}} = d_{\mathrm{TP}} = 8$, $d_{\mathrm{M}} = 15$, and $\Delta d_{\mathrm{FC}} = \Delta d_{\mathrm{M}} = \Delta d_{\mathrm{TP}} = 3$) for (d) and (e), $\mathrm{thres} = 3$, and $l = 1100$. Image size is 288 $\times$ 364 pixels.

To capture three separate object's regions, we used $n = 3$ using triple level set function $(\phi_i)_{i=1}^{3}$ that are used to embed these three initial contours as in (e)-(f). Three sets of zero level of the contours ϕ_1, ϕ_2, and ϕ_3 to segment femoral condyle, meniscus, and tibial plateau boundaries are accordingly coloured as red, green, and blue and overlaid on the original images. Although multiple initial contours overlapped with one another, the final contours in (e) are positioned on each object without any merging between the adjacent contours. However, the neighbouring contours create an overlapping region in the shared boundaries between the meniscus and the tibial plateau where the contrast is low. Hence, the framework with additional constraint is used to prevent multiple contours from overlapping with each other as depicted in (f). The corresponding area terms of the Heaviside function of these triple level set functions ϕ_1, ϕ_2, and ϕ_3 are $\sum_{p\neq 1} H_\epsilon(\phi_p) = H_\epsilon(\phi_2) + H_\epsilon(\phi_3)$, $\sum_{p\neq 2} H_\epsilon(\phi_p) = H_\epsilon(\phi_1) + H_\epsilon(\phi_3)$, and $\sum_{p\neq 3} H_\epsilon(\phi_p) = H_\epsilon(\phi_1) + H_\epsilon(\phi_2)$, respectively. Within one time step, these triple level set functions are updated. When evolving ϕ_1, another two level set functions ϕ_2 and ϕ_3 are described by their Heaviside functions $H_\epsilon(\phi_2)$ and $H_\epsilon(\phi_3)$, respectively, and vice versa. As a result, the multiple contours are evolved simultaneously to the desired boundaries of the femoral condyle, the meniscus, and the tibial plateau in a single image without any merging and overlapping between the neighbouring contours. This is confirmed by DSC and HD values computed from the segmented and manually traced contours in (c) using single and multiple level set formulation without and with the additional constraint which are summarized in the first, second, and third rows of the matrices $\begin{bmatrix} \overline{0.9155} & \overline{0.7731} & \overline{0.9430} \\ 0.9061 & 0.7734 & 0.9434 \end{bmatrix}$ and $\begin{bmatrix} \overline{5.5678} & \overline{5.9161} & \overline{5.4772} \\ 5.5678 & 6.4807 & 4.8990 \end{bmatrix}$, respectively.

3) Multiple Scale Parameters: We continued with a demonstration on how various parameters can be assigned differently for each zero level contour. In Fig. 5, we observed that different scales for each zero level contour in (e)-(f) may increase segmentation accuracy compared to (d) that produces a less accurate result. This is because the parameters' values cannot be set to be different for those three contours which are embedded in a single level set function.

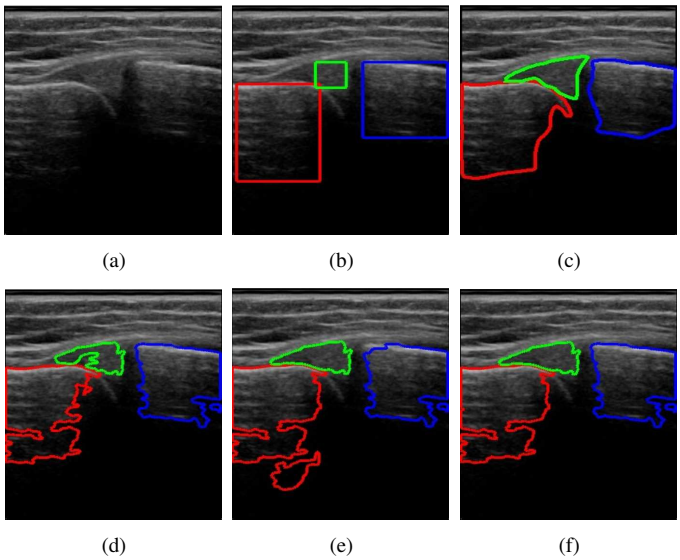

(a) (b) (c)

(d) (e) (f)

Fig. 6. (a) Original image, (b) initial, (c) manually traced, and final contours on femoral condyle (red), meniscus (green), and tibial plateau (blue) (d) with $d_{\mathrm{FC}} = d_{\mathrm{M}} = d_{\mathrm{TP}} = 13$ and $\Delta d_{\mathrm{FC}} = \Delta d_{\mathrm{M}} = \Delta d_{\mathrm{TP}} = 5$, (e) with $d_{\mathrm{FC}} = d_{\mathrm{M}} = 12$, $d_{\mathrm{TP}} = 13$, $\Delta d_{\mathrm{FC}} = 5$, and $\Delta d_{\mathrm{M}} = \Delta d_{\mathrm{TP}} = 3$, and (f) with $d_{\mathrm{FC}} = d_{\mathrm{M}} = 12$, $d_{\mathrm{TP}} = 13$, $\Delta d_{\mathrm{FC}} = \Delta d_{\mathrm{M}} = 3$, and $\Delta d_{\mathrm{TP}} = 5$. Parameters $\mathrm{thres} = 3$ and $l = 700$. Image size is 288 $\times$ 364 pixels.

In Fig. 6, we compared different choices of scale parameters in the presented multiple level set framework. Similar choice of scale parameters for each zero level contour ($d = 13$ and $\Delta d = 5$) may not produce an accurate segmentation for every object as some excluded areas are found in the segmentation outcome (d). With different scales for each zero level contour, some improvements are observed on the femoral condlye and meniscus boundaries in (e). However, we noticed that the contour on the femoral condyle are splitting and developing new areas due to the scale step being too large, i.e., $\Delta d_{\mathrm{FC}} = 5$. On the other hand, the corner area in the upper left of the tibial plateau is excluded because the scale step is too small ($\Delta d_{\mathrm{TP}} = 3$). Therefore, we set $\Delta d_{\mathrm{FC}} = 3$ for the femoral condyle and $\Delta d_{\mathrm{TP}} = 5$ for the tibial plateau to improve the segmentation accuracy. Meanwhile, the choice of Δd_{M} to be 3 or 5 is shown to produce no effect on the meniscus part. In addition, although two initial contours between the femoral condyle and the meniscus created an overlap region, we no-

This article has been accepted for publication in a future issue of this journal, but has not been fully edited. Content may change prior to final publication. Citation information: DOI 10.1109/TMI.2015.2425144, IEEE Transactions on Medical Imaging

ticed that the region vanishes after the contours have evolved. DSC and HD values for segmentation results in (d), (e), and (f) summarized accordingly in the first, second, and third rows of the matrices $\begin{bmatrix} 0.8724 & 0.7902 & 0.9244 \\ 0.8691 & 0.8543 & 0.9153 \\ 0.9137 & 0.8543 & 0.9245 \end{bmatrix}$ and $\begin{bmatrix} 4.2426 & 4.8990 & 4.8990 \\ 4.3589 & 4.5826 & 4.4721 \\ 4.2426 & 4.5826 & 4.8990 \end{bmatrix}$ confirm that different scale parameters assigned to the multiple objects of different size and shape can improve the result.

In summary, the value of d affects the accuracy of contour placement on the boundary once the kernel has found the boundary. As long as the kernel contains enough information, the position is least affected and generally accurate. In addition, the value of Δd determines the gradual increase of the kernel scale when expanding in order to detect the nearest boundary. If the value of this parameter is too large, it results in sudden changes to the scale and causes splitting contours developing new areas despite the main contour still capturing the boundary. However, if the value is too small, the contour is unable to reach some of the object region. Hence, a proper choice of both scales will result in a gradual expansion of the kernel and an accurate contour placement in the boundary.

C. Knee Meniscus Ultrasound Image Segmentation

In this subsection, we presented an application of the proposed framework to segment knee meniscus ultrasound images. Fig. 7 depicts a subset of 12 segmentation outcomes that represents variation in size, shape, and position of the objects from datasets of 70 images. The datasets that consist of 3, 4, and 5 images were available from 10, 5, and 4 subjects, respectively. For these datasets, we set $\mathrm{thres} = 3$, $l = 1000$, d_{FC}, d_{M}, and d_{TP} to be 8, 10, 12, 13, 14, or 15, and Δd_{FC}, Δd_{M}, and Δd_{TP} to be 3 or 5. Although Fig. 7 has indicated visually satisfactory results, a precise assessment to quantify the segmentation performance is of great concern. We computed DSC and HD over 70 images from contours obtained by MLREK and traced manually by the expert as shown in Fig. 8. (a) and (b), respectively. Each contour of the objects was segmented separately.

DSC values in the graph vary from 0.72 to 0.96. The value above 0.7 indicates that the two compared regions have a close similarity in area and location one and another [30]. The value greater than 0.8 indicates a better similarity area which provides more satisfactory and less inaccurate segmentation outcomes. Meanwhile, HD values are ranging from 2.65 to 8.78 pixels where a smaller value indicates that two compared shapes differ minimally each other. These values are quite small compared to image size of 288 $\times$ 364 pixels. Such a range in DSC and HD values may be influenced by the low-contrast areas and weak boundaries that are excluded in the segmentation outcomes. It may be caused by the scatter distribution of speckle noise that varies the contrast of the object ranging from low to high intensity changes. Although the local model suffers sensitivity to initialization and scale parameters [23], the results have demonstrated the robustness against various shapes, sizes, and positions of the objects.

The mean of DSC and HD measures for all objects in Table II falls in the range of 0.88 and 0.94 and of 4.41 and 5.80 pixels, demonstrating a good segmentation quality. Meanwhile, the standard deviation for DSC is between 0.02 and 0.04

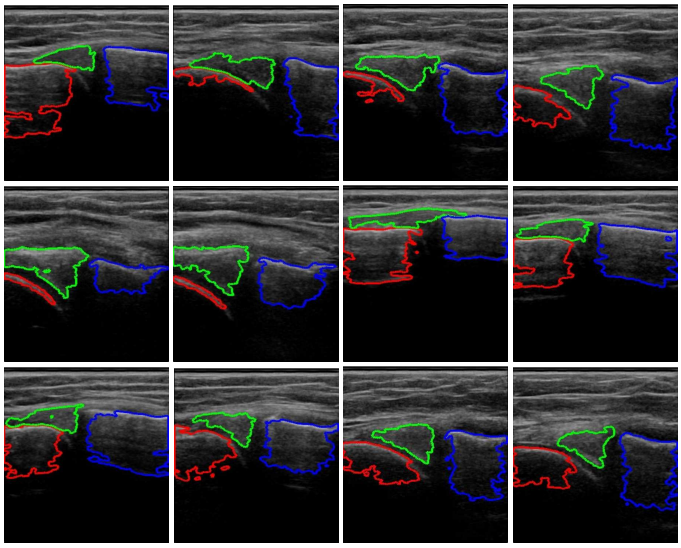

Fig. 7. A subset of 12 segmentation outcomes of the femoral condyle (red), the meniscus (green), and the tibial plateau (blue) that represents variation in size, shape, and position of the objects.

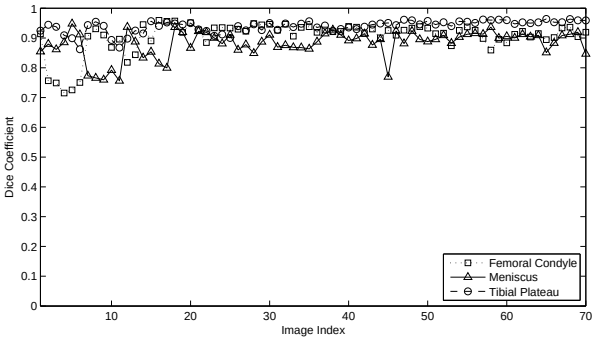

(a)

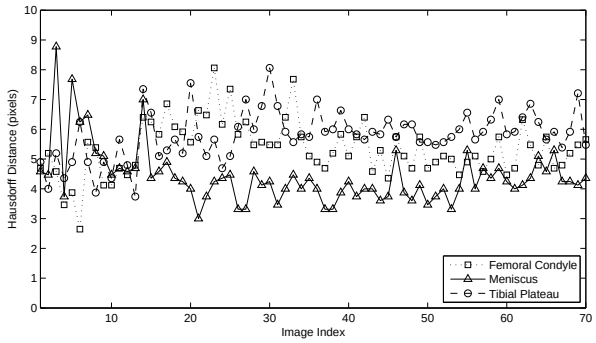

(b)

Fig. 8. (a) DSC and (b) HD measures of the femoral condyle, the meniscus, and the tibial plateau over 70 images.

and for HD is between 0.83 and 0.97 pixels, indicating that MLREK provides consistent outcomes. Intraclass correlation (ICC) values in Table II indicate a good reproducibility of the three segmentation results of the femoral condyle, the meniscus, and the tibial plateau. The Bland-Altman analysis in Fig. 9 demonstrate a good agreement between two segmentation results of the three objects where the bias is near zero

This article has been accepted for publication in a future issue of this journal, but has not been fully edited. Content may change prior to final publication. Citation information: DOI 10.1109/TMI.2015.2425144, IEEE Transactions on Medical Imaging

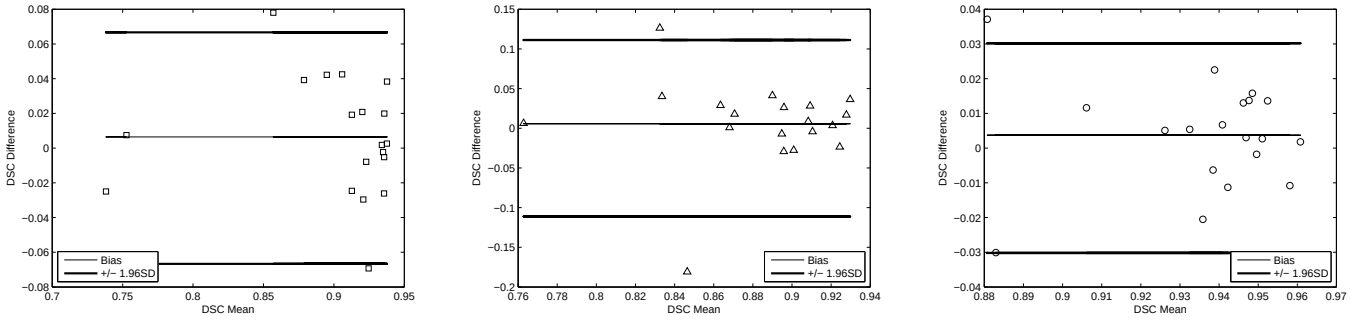

(a) (b) (c)

Fig. 9. Bland-Altman plot for DSC measures of (a) the femoral condyle, (b) the meniscus, and (c) the tibial plateau.

TABLE II
STATISTICS OF THE MEASURES

	Femoral Condyle	**Meniscus**	**Tibial Plateau**
DSC	0.91 ± 0.05	0.88 ± 0.04	0.94 ± 0.02
HD (pixels)	5.35 ± 0.91	4.41 ± 0.97	5.80 ± 0.83
ICC	0.8990	0.7040	0.8989

while the data points fall within the 95% confidence interval ($\pm$ 1.96 SD). Despite these good and consistent outcomes confirm the visually pleasing results in Fig. 7 and reflects a good agreement with its ground truth, an in-depth study of the framework application for assessment of the knee meniscus degeneration and displacement is very interesting for future work. For example, DSC values below 0.8 which have more than 20% area discrepancy may not be accurate for use in the quantification, particularly for degeneration detection. Thus, relative comparison of the meniscus area or position before and after the degeneration or displacement needs to be investigated further, where the occurrence usually takes place in a subject after a long period of time.

V. CONCLUSION

In this work, we have presented a strategy inside the variational level set method to adapt the size of the local window in order to avoid being trapped in homogeneous regions during the segmentation process. Simultaneous segmentation of femoral condyle, meniscus, and tibial plateau in an ultrasound image to determine the area and the position of the meniscus is required in order to quantify knee meniscus degeneration and displacement. We then extend this framework to simultaneous multiple object segmentation without merging and overlapping between neighbouring contours in the shared boundaries of the separate regions. We compare the proposed method to other active contour models and show the improvement in terms of segmentation performance, speed, and convergence properties that can be achieved by the proposed method. Further evaluation is performed by investigating the response of various parameters in the proposed model to segmentation results. Our experiment with varying the threshold value illustrates how it should be chosen to adapt the kernel size in order to successfully reach the concave parts. We show that it can prevent merging and overlapping and perform simultaneous segmentation of separate objects all at once in a single image. We also illustrate a flexible choice in assigning different parameter values for each contour when segmenting multiple objects. Simultaneous segmentation of the three objects on a set of knee meniscus ultrasound images indicates that MLREK produces a good and consistent segmentation outcome. While the focus of this work is on the segmentation of the knee meniscus ultrasound images, application of the framework for the assessment of the knee meniscus degeneration and displacement is of interest and left for future work.

APPENDIX
DERIVATION OF SCALABLE LOCAL REGIONAL FORCE

In obtaining our scalable local regional force, we minimize the first term of our total energy function in (7), which we restate here for convenience. Then, we substitute E_{SLR} with equation (4).

$$\begin{aligned} E(\phi) &= -\int \delta(\phi(\mathbf{y}))E_{\mathrm{SLR}}(\phi(\mathbf{x}))d\mathbf{y} \qquad (16)\\ &= -\int \delta(\phi(\mathbf{y}))\int K \times \big(|I-\mu_{\mathrm{in}}|^2 H_\epsilon(\phi(\mathbf{x})) \\ &\quad + |I-\mu_{\mathrm{out}}|^2 (1-H_\epsilon(\phi(\mathbf{x})))\big)d\mathbf{x}d\mathbf{y}. \end{aligned}$$

To compute the variation of ϕ, we replace ϕ with $\phi+\xi\psi$ by writing $E(\phi)$ as $E(\phi+\xi\psi)$.

$$\begin{aligned} E(\phi+\xi\psi) &= -\int_\Omega \delta(\phi(\mathbf{y})+\xi\psi)\int_\Omega K \qquad (17)\\ &\quad \times\Big(|I(\mathbf{x})-\mu_{\mathrm{in}}|^2 H_\epsilon(\phi(\mathbf{x})+\xi\psi) \\ &\quad + |I(\mathbf{x})-\mu_{\mathrm{out}}|^2 (1-H_\epsilon(\phi(\mathbf{x})+\xi\psi))\Big)d\mathbf{x}d\mathbf{y}. \end{aligned}$$

The first variation of E is derived to obtain the optimal ϕ. The partial derivative of E is taken with respect to ξ for $\xi=0$.

$$\begin{aligned} \frac{\partial E(\phi+\xi\psi)}{\partial\xi} &= -\Big(\int \delta(\phi(\mathbf{y}))\int \psi\delta(\phi(\mathbf{x})) \qquad (18)\\ &\quad K\times\big(|I-\mu_{\mathrm{in}}|^2-|I-\mu_{\mathrm{out}}|^2\big)d\mathbf{x}d\mathbf{y} \\ &\quad +\psi\int\delta'(\phi(\mathbf{y}))\int K\cdot\big(|I-\mu_{\mathrm{in}}|^2 H_\epsilon(\phi(\mathbf{x})) \\ &\quad + |I-\mu_{\mathrm{out}}|^2(1-H_\epsilon(\phi(\mathbf{x})))\big)d\mathbf{x}d\mathbf{y}\Big). \end{aligned}$$

This article has been accepted for publication in a future issue of this journal, but has not been fully edited. Content may change prior to final publication. Citation information: DOI 10.1109/TMI.2015.2425144, IEEE Transactions on Medical Imaging

On the zero level set function, $\delta'(\phi)$ evaluates to zero, thus this term can be omitted. We use the chain rule and plug in $\xi = 0$ to obtain $\frac{\partial E}{\partial \phi}$.

$$\begin{aligned} \frac{\partial E}{\partial \phi} &= -\int \delta(\phi(\mathbf{y})) \int \psi\delta(\phi(\mathbf{x})) \\ & \quad K \times \left(|I - \mu_{\text{in}}|^2 - |I - \mu_{\text{out}}|^2 \right) d\mathbf{x} d\mathbf{y}. \end{aligned} \tag{19}$$

For all ψ, the partial derivative is zero, then we obtain $\frac{\partial E}{\partial \phi} = 0$. Hence, the gradient flow equation is given as follows

$$\begin{aligned} \frac{\partial \phi}{\partial t} &= \delta(\phi(\mathbf{y})) \int \delta(\phi(\mathbf{x})) \\ & \quad K \times \left(|I - \mu_{\text{in}}|^2 - |I - \mu_{\text{out}}|^2 \right) d\mathbf{x} \\ &= \delta(\phi(\mathbf{y})) F_{\text{SLR}}(\phi(\mathbf{x})) \end{aligned} \tag{20}$$

REFERENCES

[1] D. Pereiraya, B. Peleteiroyza, J. Arajoyza, J. Brancoxa, R. A. Santoska, and E. Ramos, "The effect of osteoarthritis definition on prevalence and incidence estimates: a systematic review," *Osteoarthr. Cartil.*, vol. 19, pp. 1270–1285, Aug. 2011.

[2] H. J. Braun and G. E. Gold, "Diagnosis of osteoarthritis: Imaging," *Bone*, vol. 51, pp. 278–288, Aug. 2012.

[3] F. W. Roemer, M. D. Crema, S. Trattnig, and A. Guermazi, "Advances in imaging of osteoarthritis and cartilage," *Radiology*, vol. 260, no. 2, pp. 332–354, Aug. 2011.

[4] D. J. Hunter, Y. Q. Zhang, X. Tu, M. LaValley, J. B. Niu, S. Amin, A. Guermazi, H. Genant, D. Gale, and D. T. Felson, "Change in joint space width: Hyaline articular cartilage loss or alteration in meniscus?," *Arthritis Rheum.*, vol. 54, no. 8, pp. 2488–2495, Aug. 2006.

[5] S. Amin, M. P. LaValley, A. Guermazi, M. Grigoryan, D. J. Hunter, M. Clancy, J. Niu, D. R. Gale, and D. T. Felson, "The relationship between cartilage loss on magnetic resonance imaging and radiographic progression in men and women with knee osteoarthritis," *Arthritis Rheum.*, vol. 52, no. 10, pp. 3152–3159, Oct. 2005.

[6] D. J. Hunter, R. Buck, E. Vignonk, F. Eckstein, K. Brandt, S. A. Mazzucayy, B. T. Wymanx, I. Otternesszz, and M. P. Hellio Le Graverandx, "Relation of regional articular cartilage morphometry and meniscal position by MRI to joint space width in knee radiographs," *Osteoarthr. Cartil.*, vol. 17, pp. 1170–1176, Apr. 2009.

[7] P. Dodin, J.-P. Pelletier, J. Martel-Pelletier, and F. Abram, "Automatic human knee cartilage segmentation from 3-D magnetic resonance images," *IEEE Trans. Biomed. Eng.*, vol. 57, no. 11, pp. 2699–2711, Nov. 2010.

[8] J. Fripp, S. Crozier, S. K. Warfield, and S. Ourselin, "Automatic segmentation and quantitative analysis of the articular cartilages from magnetic resonance images of the knee," *IEEE Trans. Med. Imag.*, vol. 29, no. 1, pp. 55–63, Jan. 2010.

[9] J. Folkesson, E. B. Dam, O. F. Olsen, P. C. Pettersen, and C. Christiansen, "Segmenting articular cartilage automatically using a voxel classication approach," *IEEE Trans. Biomed. Eng.*, vol. 26, no. 1, pp. 106–115, Jan. 2007.

[10] J. Tang, S. Millington, S. T. Acton, J. Crandall, and S. Hurwitz, "Surface extraction and thickness measurement of the articular cartilage from MR images using directional gradient vector flow snakes," *IEEE Trans. Biomed. Eng.*, vol. 53, no. 5, pp. 896–907, May 2006.

[11] S. Tummala, M. Nielsen, M. Lillholm, C. Christiansen, and E. B. Dam, "Automatic quantification of tibio-femoral contact area and congruengity," *IEEE Trans. Med. Imag.*, vol. 31, no. 7, pp. 1404–1412, Jul. 2012.

[12] J. Fripp, P. Bourgeat, C. Engstrom, S. Ourselin, S. Crozier, and O. Salvado, "Automated segmentation of the menisci from MR images," in *Proc. IEEE Int. Symp. Biomed. Imag.*, Jun. 2009, pp. 510–513.

[13] I. Boniatis, G. Panayiotakis, and E. Panagiotopoulos, "A computer-based system for the discrimination between normal and degenerated menisci from magnetic resonance images," in *Proc. IEEE Int. Workshop Imag. Syst. Techn.*, Sep. 2008, pp. 510–513.

[14] M. S. Swanson, J. W. Prescott, T. M. Best, K. Powell, R. D. Jacksonk, F. Haq, and M. N. Gurcan, "Semi-automated segmentation to assess the lateral meniscus in normal and osteoarthritic knees," *Osteoarthr. Cartil.*, vol. 18, no. 3, pp. 344–353, Oct. 2010.

[15] A. M. Abraham, I. Goff, M. S Pearce, R. M Francis, and F. Birrell, "Reliability and validity of ultrasound imaging of features of knee osteoarthritis in the community," *BMC Muscuskelet. Disord.*, vol. 70, no. 12, pp. 1471–2474, Apr. 2011.

[16] S. Saarakkala, P. Waris, V. Waris, I. Tarkiainen, E. Karvanen, J. Aarnio, and J. M. Koski, "Diagnostic performance of knee ultrasonography for detecting degenerative changes of articular cartilage," *Osteoarthr. Cartil.*, vol. 20, pp. 376–381, Apr. 2012.

[17] C. Acebes, F. I. Romero, M. A. Contreras, I. Mahillo, and G. Herrero-Beaumont, "Dynamic ultrasound assessment of medial meniscal subluxation in knee osteoarthritis," *Rheumatology*, vol. 52, pp. 1443–1447, Apr. 2013.

[18] A. Iagnocco, "Imaging the joint in osteoarthritis: A place for ultrasound?," *Best Pract. Res. Clin. Rheumatol.*, vol. 24, pp. 27–38, 2010.

[19] I. Moller, D. Bong, E. Naredo, E. Filippucci, I. Carrasco, C. Moragues, and A. Iagnocco, "Ultrasound in the study and monitoring of osteoarthritis," *Osteoarthr. Cartil.*, vol. 16, pp. S4–S7, 2008.

[20] T. F. Chan and L. A. Vese, "Active contours without edges," *IEEE Trans. Image Process.*, vol. 10, no. 2, pp. 266–277, Feb. 2001.

[21] C. Li, C. Kao, C. Gore, and Z. Ding, "Minimization of region scalable fitting energy for image segmentation," *IEEE Trans. Image Process.*, vol. 17, no. 10, pp. 1940–1949, Oct. 2008.

[22] V. Casseles, R. Kimmel, and G. Sapiro, "Geodesic active contours," *Int. J. Comput. Vis.*, vol. 22, no. 1, pp. 6179, 1997.

[23] S. Lankton and A. Tanenbaum, "Localizing region-based active contours," *IEEE Trans. Image Process.*, vol. 17, no. 11, pp. 2029–2039, Nov. 2008.

[24] C. Darolti, A. Mertins, C. Bodensteiner, and U. G. Hoffman, "Local region descriptor for active contours evolution," *IEEE Trans. Image Process.*, vol. 17, no. 12, pp. 2275–2288, Dec. 2008.

[25] S. Phumeechanya, C. Pluempitiwiriyawej, and S. Thongvigitmanee, "Active contour using local regional information on extendable search lines (LRES) for image segmentation," *IEICE Trans. Inf. Syst.*, vol. E-93, no. 6, pp. 1625–1635, Jun. 2010.

[26] L. A. Vese and T. F. Chan, "A multiphase level set framework for image segmentation using the Mumford and Shah model," *Int. J. Comput. Vis.*, vol. 50, no. 3, pp. 271–293, 2002.

[27] T. Brox and J. Weickert, "Level set segmentation with multiple regions," *IEEE Trans. Image Process.*, vol. 15, no. 10, pp. 2029–2039, Oct. 2006.

[28] H. K. Zhao, T. Chan, B. Merriman, and S. Osher, "A variational level set approach to multiphase motion," *J. Comp. Phys.*, vol. 127, pp. 179–195, 1996.

[29] E. Naredo, F. Cabero, M. J. Palop, P. Collado, A. Cruz, and M. Crespo, "Ultrasonographic findings in knee osteoarthritis: A comparative study with clinical and radiographic assessment," *Osteoarthr. Cartil.*, vol. 13, no. 7, pp. 568–574, 2005.

[30] A. P. Zijdenbos, B. M. Dawant, R. A. Margolin, and C. Palmer, "Morphometric analysis of white matter lesions in MR images: Method and validation," *IEEE Trans. Med. Imag.*, vol. 13, no. 4, pp. 716–724, Dec. 1994.